The carbon cycle of southeast Australia during 2019-2020: Drought, fires and subsequent recovery

B. Byrne[1], J. Liu[1,2], M. Lee[1], Y. Yin[2], K. W. Bowman[1,3], K. Miyazaki[1], A. J. Norton[1], J. Joiner[4], D. F. Pollard[5], D. W. T. Griffith[6], V. A. Velazco[6]*, N. M. Deutscher[6], N. B. Jones[6], and C. Paton-Walsh[6]

[1]Jet Propulsion Laboratory, California Institute of Technology, Pasadena, CA, USA
[2]Division of Geological and Planetary Sciences, California Institute of Technology, Pasadena, CA, USA
[3]Joint Institute for Regional Earth System Science and Engineering, University of California, Los Angeles, USA
[4]Laboratory of Atmospheric Chemistry and Dynamics, NASA Goddard Space Flight Center, Greenbelt, MD, USA
[5]National Institute of Water and Atmospheric Research Ltd (NIWA), Lauder, New Zealand
[6]Centre for Atmospheric Chemistry, School of Earth, Atmospheric and Life Sciences, University of Wollongong, Wollongong, New South Wales, Australia
*Now at Deutscher Wetterdienst, German Meteorological Service Meteorological Observatory, Hohenpeissenberg Albin-Schwaiger-Weg 10 82383, Germany

Corresponding author: Brendan Byrne, brendan.k.byrne@jpl.nasa.gov, @BKAByrne

The carbon cycle of southeast Australia during 2019–2020: Drought, fires and subsequent recovery

B. Byrne[1], J. Liu[1,2], M. Lee[1], Y. Yin[2], K. W. Bowman[1,3], K. Miyazaki[1], A. J. Norton[1], J. Joiner[4], D. F. Pollard[5], D. W. T. Griffith[6], V. A. Velazco[6,*], N. M. Deutscher[6], N. B. Jones[6], and C. Paton-Walsh[6]

[1]Jet Propulsion Laboratory, California Institute of Technology, Pasadena, CA, USA
[2]Division of Geological and Planetary Sciences, California Institute of Technology, Pasadena, CA, USA
[3]Joint Institute for Regional Earth System Science and Engineering, University of California, Los Angeles, USA
[4]Laboratory of Atmospheric Chemistry and Dynamics, NASA Goddard Space Flight Center, Greenbelt, MD, USA
[5]National Institute of Water and Atmospheric Research Ltd (NIWA), Lauder, New Zealand
[6]Centre for Atmospheric Chemistry, School of Earth, Atmospheric and Life Sciences, University of Wollongong, Wollongong, New South Wales, Australia
[*]Now at Deutscher Wetterdienst, German Meteorological Service Meteorological Observatory, Hohenpeissenberg Albin-Schwaiger-Weg 10 82383, Germany

Key Points:

- 113–236 TgC of CO_2 were released through biomass burning, and 19–52 TgC of CO_2 through reduced ecosystem productivity.
- Transition to cool-wet conditions resulted in robust recovery for unburned ecosystems but not for burned forests.
- Space-based remote sensing of trace gases and MODIS reflectances provide strong constraints on carbon cycle anomalies produced by extreme events.

Corresponding author: Brendan Byrne, `brendan.k.byrne@jpl.nasa.gov`

Abstract

2019 was the hottest and driest year on record for southeast Australia leading to bushfires of unprecedented extent between November 2019 and January 2020. In this study, we utilize space-based measurements of trace gases (TROPOspheric Monitoring Instrument X_{CO}, Orbiting Carbon Observatory 2 X_{CO_2}) and up-scaled GPP (FluxSat GPP) to quantify the carbon cycle anomalies resulting from drought and fire in southeast Australia during the 2019–2020 growing season. We find that biomass burning emissions released 113–236 TgC of CO_2 while drought and fire induced anomalies in net ecosystem exchange reduced growing season carbon uptake by an additional 19–52 TgC of CO_2. These carbon losses were concentrated during the spring and early summer, when hot-dry conditions were most severe. A shift to cooler conditions and above average rainfall during February is found to result in a partial recovery and greening in unburned ecosystems. However, fire impacted areas had continued suppressed productivity for the remainder of the growing season. This study showcases the capability of combining observations from multiple satellites to monitor the carbon and ecosystem anomalies resulting from extreme events.

Plain Language Summary

Extreme climate events can have a large impacts on the carbon cycle of ecosystems. Droughts suppress photosynthesis, reducing the amount of CO_2 absorbed from the atmosphere, and fires release CO_2 to the atmosphere through combustion. In this study, we use satellite observations to quantify the disruption to the carbon cycle due to drought and bushfires in southeast Australia during 2019–2020. The drought and bushfires resulted in a carbon loss from these ecosystems that is greater than Australia's annual fossil fuel emissions, although the carbon is expected to be drawn back into these ecosystems as the forests recover. This study highlights our ability to track the carbon cycle from space.

1 Introduction

Extreme drought and heat events have major impacts on the carbon cycle of terrestrial ecosystems, and can result in single-year carbon losses equal to many years of carbon sequestration (Ciais et al., 2005; Bastos et al., 2014). Hot-dry conditions can directly suppress both gross primary productivity (GPP) and ecosystem respiration (TER), with greater suppression of GPP leading to carbon loss (Reichstein et al., 2007; Sippel et al., 2018). These conditions can also precondition secondary carbon cycle disturbances, such as fires (D. M. J. S. Bowman et al., 2009; Abram et al., 2020), which in turn lead to increased carbon loss. Impacted ecosystems often experience legacy effects after the extreme events have passed, which can impact the carbon cycling for years (Frank et al., 2015). Post-drought reduced growth has been observed for 1–4 years (Anderegg et al., 2015; Wu et al., 2018), while even longer term legacy effects have been found for fires, with many forests found to have continued carbon loss for a decade post-fire (Amiro et al., 2010; Goulden et al., 2011).

The impact of extreme drought and heat events on ecosystems are complex and challenging to monitor. Ecosystem responses are sensitive to the specific characteristics of the event, such as the intensity and timing (Bastos et al., 2014; Frank et al., 2015; De Boeck et al., 2011; Denton et al., 2017), and legacy effects from previous disturbances (Longo et al., 2020). Different ecosystems may also respond differently to the same event. For example, Zhang et al. (2016) found that non-forest ecosystems had large structural changes in response to the 2003 European drought, while forests mainly showed physiological responses. Thus, to fully understand the impact of extreme events on the carbon cycle, we must quantify carbon cycle anomalies with attention to spatial and temporal details.

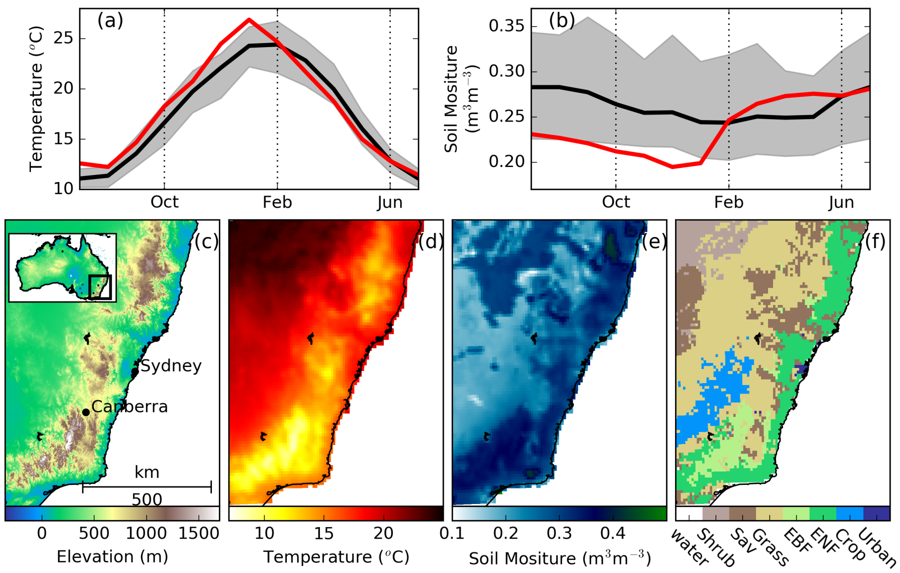

Figure 1. Climate and Geography of southeast Australia. ERA4 Land (a) soil temperature and (b) soil moisture over southeast Australia for 2010–2018 (black line, shaded area showing the range) and 2019–2020 (red). (c) Surface elevation, (d) 2010–2018 mean soil temperature, (e) 2010–2018 mean soil moisture, and (f) MODIS IGBP vegetation type.

Expanding space-based observing systems of carbon-cycle-relevant quantities are allowing for finer scale quantification of carbon cycle perturbations and more detailed understanding of the response of ecosystems to extreme drought, heat and fire (Byrne, Liu, Lee, et al., 2020; Byrne, Liu, Bloom, et al., 2020; Yin et al., 2020; Turner et al., 2020). In this study, we utilize space-based observations to provide a comprehensive analysis of the carbon cycle perturbations due to extreme drought, heat and fire during the 2019–2020 growing season in southeast Australia (Fig. 1). This region has a highly variable climate (Harris & Lucas, 2019; King et al., 2020) and has been predicted to have more frequent heat and fire events with climate change (Perkins-Kirkpatrick & Gibson, 2017; Abatzoglou et al., 2019; Dowdy et al., 2019; Di Virgilio et al., 2019). Thus, understanding the response of ecosystems in southeast Australia to extreme drought, heat and fire is critical for understanding how the carbon balance of this regions will evolve under climate change.

Southeast Australia has been in drought since 2017, with the 2017–2019 period having the largest three year rainfall deficit since 1900 (King et al., 2020). These conditions have been most extreme during 2019, which was the hottest and driest year recorded in southeast Australia (Abram et al., 2020; Bureau of Meteorology, 2020), preconditioning one of the worst bushfires seasons in recorded history (Nolan et al., 2020; King et al., 2020; Deb et al., 2020; Boer et al., 2020; Ward et al., 2020; Collins et al., 2021). These extreme conditions subsided in early February 2020 with heavy rainfall and cooler conditions, which persisted throughout the austral autumn. This combination of drought and fire, followed by heavy rainfall imparts a large and complex perturbation on the carbon cycle of the region and impacted evergreen broadleaf forests (EBFs) that cover much of the southeast coast, evergreen needleleaf forests (ENFs) that occupy more mountainous ecosystems near the coast, particularly in the south, and more arid savanna, grassland and cropland ecosystems further inland (Fig. 1).

We combine observations from multiple satellites to quantify the carbon cycle anomalies within southeast Australia. We employ TROPOspheric Monitoring Instrument (TROPOMI) CO column abundance measurements (Landgraf et al., 2016; Borsdorff et al., 2018) to quantify biomass burning emissions. Anomalies in net ecosystem exchange (NEE, which is defined as the residual between ecosystem respiration and GPP) are obtained by combining top-down constraints on net surface-atmosphere CO_2 fluxes from column-averaged dry-air mole fractions of CO_2 (X_{CO_2}) measurements from the Orbiting Carbon Observatory 2 (OCO-2) (O'Dell et al., 2012; Crisp et al., 2012) with estimates of GPP anomalies from FluxSat (Joiner & Yoshida, 2020), which produces GPP from MODIS reflectances trained against FLUXNET sites.

The combination of these newly available observations offers a unique opportunity to monitor individual components of the carbon cycle anomalies across southeast Australia during 2019–2020. Specifically, we aim to ask: How much CO_2 was released to the atmosphere due to drought and biomass burning, respectively? How did this event impact EBFs, ENFs, and non-forest ecosystems differently? And what were the differences in carbon cycle perturbations between burned and unburned ecosystems? To that end, we first quantify biomass burning emissions of CO from the TROPOMI observations, which are then converted to CO_2 emissions (Sec. 3.1). Then, an anomaly in atmospheric CO_2 (ΔCO_2) is derived from the OCO-2 measurements (Sec. 3.2). This top-down constraint is then combined with estimates of GPP anomalies from FluxSat to derive NEE anomalies over the 2019–2020 growing season (Sec. 3.3). We then synthesize these estimates and present the evolution of carbon cycle anomalies over the 2019–2020 growing season (Sec. 4). This is followed by a discussion of our biomass burning emission estimates in the context of previous bottom up estimates (Sec. 5.1), the uncertainties and remaining challenges in estimating carbon fluxes from extreme events (Sec 5.2), and the implications of this extreme event for the carbon cycle of southeast Australia (Sec. 5.3). Finally, we provide our conclusions in Sec. 6.

2 Environmental and Geographical data

Environmental and geographical data are used to help interpret the carbon cycle anomalies. We examine the covariations of carbon cycle anomalies with variations in soil temperature and soil moisture from ERA5-Land reanalysis (Munoz Sabater, 2019), generated using Copernicus Climate Change Service Information 2020. For this analysis, we calculate the area-weighted soil moisture and temperature over the top 1 m of soil. Vegetation land cover are obtained from the MODIS land cover dataset (MCD12C1) (Friedl & Sulla-Menashe, 2015) and elevation data is obtained from ETOPO1 (Amante & Eakins, 2009).

3 CO_2 Flux Estimates

Figure 2 shows a schematic diagram of the methods used to estimate biomass burning and anomalies in NEE (ΔNEE). Biomass burning CO_2 emissions are estimated from TROPOMI X_{CO} measurements (Sec. 3.1). First, emissions of CO are estimated through flux inversion analyses that assimilate TROPOMI X_{CO} measurements. Then CO emissions are converted to CO_2 emissions using emission scaling factors.

Estimates of ΔNEE are obtained through combining several different data sources. First, we infer a top-down CO_2 anomaly signal (ΔX_{CO_2}) due to anomalies in biosphere-atmosphere CO_2 fluxes (Sec. 3.2). Then we subtract the ΔX_{CO_2} signal due to biomass burning emissions, giving ΔX_{CO_2} due to ΔNEE. This provides a constraint on the magnitude of ΔNEE. Finally, we estimate spatiotemporal structure of ΔNEE by combining the atmospheric CO_2 constraints with FluxSat GPP (Sec. 3.3). Note that the CO_2 flux and atmospheric X_{CO_2} are related to fluxes using a chemical transport model (Sec. 3.1.1).

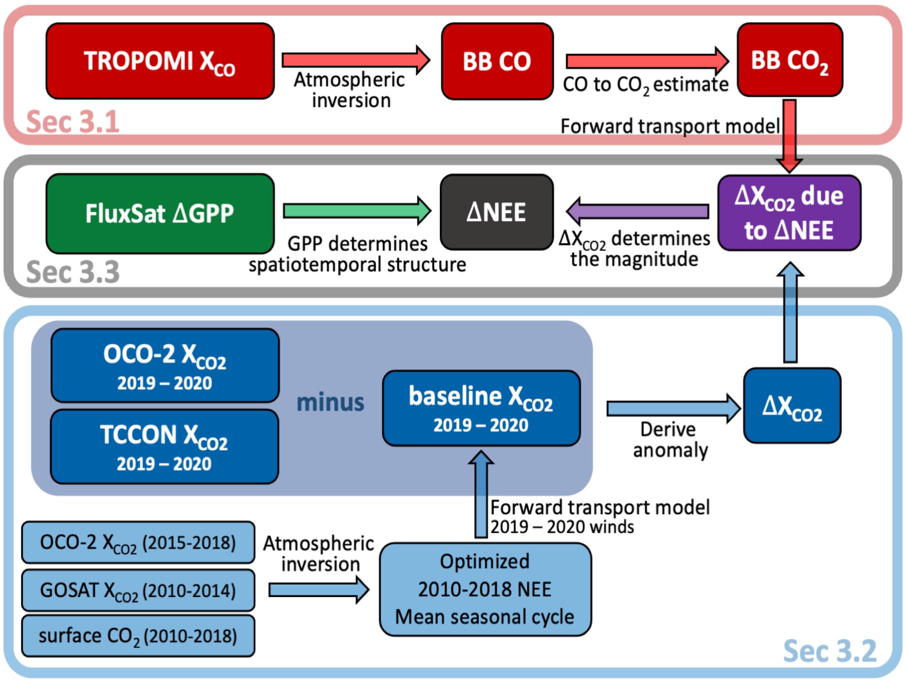

Figure 2. Schematic diagram of the method used to derive biomass burning and ΔNEE CO_2 fluxes. Biomass burning emissions are based on TROPOMI X_{CO} measurements (shown in red). CO_2-based estimates of ΔX_{CO_2} are estimated from measurements of atmospheric CO_2 (shown in blue). First, NEE fluxes over 2010-2018 are estimated through flux inversion analysis (shown in light blue). Combining the mean NEE seasonal cycle over this period with a chemical transport model, we simulate the expected 2019–2020 baseline atmospheric CO_2 fields given climatological fluxes. Then, the difference between the actual 2019–2020 measurements and the expected X_{CO_2} gives the anomaly in atmospheric X_{CO_2} (shown in blue shaded area). ΔNEE is then estimated from combining all of the constraints. The spatiotemporal structure of ΔNEE is based on FluxSat GPP (shown in green), while the magnitude is derived from combining the top-down and biomass-burning-derived ΔCO_2 estimates (shown in purple).

Atmospheric chemical transport simulations and flux inversions are performed with the Greenhouse Gas Framework - Flux (GHGF-Flux) inversion system. GHGF-Flux is a flux inversion system developed under the NASA Carbon Monitoring System Flux (CMS-Flux) project (https://cmsflux.jpl.nasa.gov), and inherits the chemistry transport model from the GEOS-Chem and the adjoint model from the GEOS-Chem adjoint (Henze et al., 2007; Liu et al., 2014). Chemical transport is driven by the Modern Era Retrospective Analysis for Research and Applications, Version 2 (MERRA-2) meteorology produced with version 5.12.4 of the Goddard Earth Observing System (GEOS) atmospheric data assimilation system (Gelaro et al., 2017). To perform tracer transport, these fields are regridded to the desired horizontal resolution and archived with a temporal resolution of three hours except for surface quantities and mixing depths, which have a temporal resolution of one hour. Flux inversions are performed using 4-D variational assimilation (4D-Var), with the details provided in the subsections.

3.1 Biomass burning emissions

Atmospheric CO inversions have been shown to be an effective top-down approach for estimating fire carbon emissions (Yin et al., 2015, 2016, 2020; Liu et al., 2017; Zheng et al., 2019). Here, we perform atmospheric CO inversions to estimate biomass burning emissions by assimilating TROPOMI retrievals of (X_{CO}). TROPOMI is a grating spectrometer aboard ESA's Sentinel-5 Precursor (S-5P) satellite that measures Earth reflected radiances (Veefkind et al., 2012). CO total column densities are retrieved in the shortwave infrared (around 2.3 μm) using the Shortwave Infrared CO Retrieval (SICOR) algorithm (Landgraf et al., 2016). Retrieved CO total column densities are then converted to dry-air mole fractions of CO (X_{CO}) using the dry-air surface pressure and hypsometric equation. The column averaging kernel is similarly converted to mole-fraction space.

Biomass burning CO emissions are estimated using one-way nested flux inversions over Australia ($100° - 177.5°$ E, $0° - 60°$ S) at $0.5° \times 0.625°$ spatial resolution. Nested flux inversions are performed from 5 Nov 2019 through 14 Jan 2020 (to cover the period with the majority of fires) and assimilate TROPOMI X_{CO} super-obs (aggregated observations) to optimize scaling factors for each gridcell over the entire period. Details on the inversion configuration are provided in Appendix A. The posterior scale factors are then applied over the entire Oct–May time period (note that biomass burning emissions are small outside of the inversion period).

Eight nested flux inversions are performed, which vary in prior biomass burning emissions, quantities optimized, and boundary conditions (Table 1). Differences in flux inversion configuration are employed to test the sensitivity of posterior fluxes to the inversion set-up. We employ either Global Fire Emissions Database version 4 (GFED4.1s) (van der Werf et al., 2017) or Global Fire Assimilation System (GFAS) (Kaiser et al., 2012) CO fluxes as prior biomass burning emissions. GFED4.1s provides estimates of biomass burning using MODIS 500 m burned area (Giglio et al., 2013), 1 km thermal anomalies, and 500 m surface reflectance observations to statistically estimate burned area associated with small fires (Randerson et al., 2012). GFAS v1.2 provides estimates of daily biomass burning emissions by assimilating MODIS fire radiative power observations (Di Giuseppe et al., 2018; Kaiser et al., 2012). For both datasets, we incorporate the impact of the diurnal cycle based on Mu et al. (2011). The inversions also differ by either prescribing or optimizing diurnal variations on biomass burning emissions. Finally, inversions are either run using boundary conditions from a global TROPOMI flux inversion or with these boundary conditions adjusted by adding 10 ppb (roughly equivalent to the mean data-model difference) at all levels and times to test the sensitivity of nested CO inversion to lateral boundary conditions.

Video 1 [Figure 3/supp Video 1 in pre-print] shows the spatial distribution of the mean posterior fluxes and X_{CO} measurements across southeast Australia. Biomass burn-

Table 1. Flux inversion set-up for the eight nested TROPOMI CO flux inversions.

Inversion	prior BB emissions	Boundary conditions	Optimized fluxes
1	GFED4.1s	optimized	mean BB diurnal BB
2	GFED4.1s	optimized	mean BB
3	GFED4.1s	opt + 10 ppb	mean BB diurnal BB
4	GFED4.1s	opt + 10 ppb	mean BB
5	GFASv1.2	optimized	mean BB diurnal BB
6	GFASv1.2	optimized	mean BB
7	GFASv1.2	opt + 10 ppb	mean BB diurnal BB
8	GFASv1.2	opt + 10 ppb	mean BB

ing emissions were most concentrated in forest ecosystems along the coast, where EBFs are most widespread, and further inland along the border between New South Wales and Victoria, where ENFs are most common. Posterior CO emissions are increased for all inversion configurations, with a posterior mean CO emission estimate of 15.6 TgC (range: 9.7–24.3 TgC), relative to prior emission estimates of 11.4 TgC for GFED and 5.8 TgC for GFAS over the growing season. The largest source of spread among posterior fluxes is due to the prior biomass burning flux employed, with GFED-based inversions giving larger posterior emissions than GFAS-based inversions (see Figure S2 in the supporting information).

The performance of the nested CO flux inversions are evaluated by comparing the posterior CO fields with the TROPOMI X_{CO} measurements and independent X_{CO} measurements from the nearby Wollongong (Griffith et al., 2014) and Lauder (Pollard et al., 2019, 2017) Total Column Carbon Observing Network (TCCON) (Wunch et al., 2011) sites, and the Cross-track Infrared Sounder (CrIS). CrIS is a Fourier Transform Spectrometer aboard Suomi-NPP satellite and has a spectral resolution of 0.625 cm^{-1} and a ground pixel diameter of 14 km at nadir. CrIS and TROPOMI make collocated measurements because Suomi-NPP and Sentinel 5p are in a tandem orbit with a roughly 10 min separation. However, CrIS takes measurements in both day and night. The retrieval of CO uses the MUlti-SpEctra, MUlti-SpEcies, Multi-SEnsors (MUSES) algorithm (Fu et al., 2016) that is based on the optimal estimation method with heritage from the Tropospheric Emission Spectrometer (TES) (K. W. Bowman et al., 2006). We generate X_{CO} measurements from version 1.8 of the L2 tropospheric CO profile product, and compare posterior CO fields against daytime and nighttime X_{CO} measurements separately.

As trace gas emissions from fires are impacted by pyroconvective motions (that are not well represented in chemical transport models), we evaluate the posterior fluxes with two sets of model runs that release the CO emissions at different model levels. In one set of runs, we release the emissions at the surface (as was done in the inversion), while in the second set we release CO emissions at the injection height (mean altitude of maximum injection) simulated by a plume rise model (IS4FIRES) (Rémy et al., 2017), which was provided with the GFAS emission data. Here we provide a brief summary of the evaluation, while a detailed evaluation of the flux inversions is presented in Text S1 of the

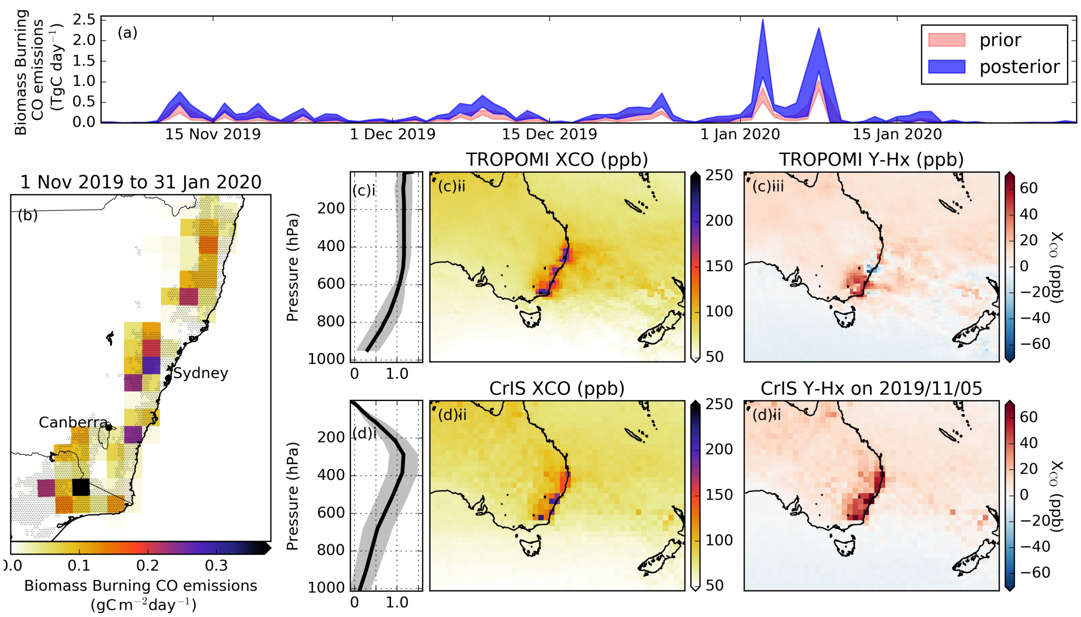

Figure 3. [See Video 1](a) Timeseries showing the range of prior (red) and posterior (blue) biomass burning CO emissions over southeast Australia. (b) Mean posterior biomass burning emissions at 0.5° × 0.625° spatial resolution. Hatching indicates the locations of forested areas. (c) TROPOMI (i) mean X_{CO} column averaging kernel, (ii) mean X_{CO} and (iii) posterior data-model mismatch at 0.5° × 0.625° spatial resolution. (d) CrIS (i) mean X_{CO} column averaging kernel, (ii) mean X_{CO} and (iii) posterior data-model mismatch at 1.0° × 1.0° spatial resolution.

supporting information. Posterior fluxes generally show better agreement with the TROPOMI, TCCON and CrIS measurements. This is true for all measurements and a subset of measurements that are biomass-burning-sensitive. However, posterior CO fluxes tend to underestimate X_{CO} for biomass-burning-sensitive measurements (but less so than the prior). This residual mismatch is likely related to transport model errors, as the modeled observations often show differences in plume structure (Video 1/Fig. 3). Furthermore, the transport model underestimates vertical motions around the bushfires, which were impacted by pyroconvection. The impact of weak modeled vertical motions can be seen in Video 1c,d/Figure 3c,d. The column averaging kernel for TROPOMI shows greater sensitivity to CO between 400 hPa and the surface, while CrIS shows greater sensitivity to CO in the upper troposphere. Both TROPOMI and CrIS show mean X_{CO} mole fractions greater than 200 ppb in southeast Australia for the duration of the biomass burning over Nov–Jan. However, posterior data-model mismatches are much less positive for TROPOMI than for CrIS, implying that vertical motions are underestimated and the CO emissions do not reach the upper troposphere to the levels observed.

Finally, to estimate CO_2 biomass burning emissions we apply the ratio of CO_2 to CO emission factors (that are constant in time). We apply the emission factors from the biomass burning database used as the prior (e.g., either GFAS or GFED). The emission ratios are variable by vegetation type, but aggregating for fires across Australia gives effective CO_2/CO emission ratios of 12.01 for GFED and 11.30 for GFAS. Differences are primarily driven by differences in emission factors for forest emissions, but are within the natural variation of emission factors reported by Akagi et al. (2011) (see Text S2 and Fig. S4 in the supporting information).

3.1.1 *Atmospheric ΔCO_2 signal simulation*

We simulate the biomass burning X_{CO_2} anomaly signal ($\Delta X_{CO_2\ BB}$) by running the nested chemical transport model. The $\Delta X_{CO_2\ BB}$ signal is calculated by performing simulations with climatological fluxes and with the climatological fluxes plus the biomass burning estimates, then taking the difference between these two simulations at the OCO-2 and TCCON measurements locations to isolate the signal due to biomass burning. We simulate OCO-2 good-quality land (land glint and land nadir) and ocean glint super-obs (aggregated to $0.5°\times0.5°$ resolution grids following Liu et al. (2017), with the additional requirement that there must be a minimum of three OCO-2 observations within each $0.5°\times0.5°$ grid box per track). For TCCON measurements, we only simulate measurements between 11 a.m. and 3 p.m. local time with solar zenith angles less than 70°.

3.2 Top-down ΔCO_2 signal

The top-down estimate of ΔX_{CO_2} are calculated based on the data-model difference between OCO-2 and TCCON measurements and simulated CO_2 fields based on climatological NEE emissions.

Climatological NEE fluxes are generated through CO_2 flux inversion analyses. We generate climatological NEE fluxes as the average over the period 2010–2018. Fluxes over 2010–2014 are taken as the mean GOSAT+surface+TCCON inversion of Byrne, Liu, Lee, et al. (2020). To generate climatological fluxes over 2015-2018, we perform a flux inversion at $4°\times5°$ assimilating OCO-2 measurements and surface-based CO_2 measurements concurrently and use the identical inversion set-up to Byrne, Liu, Lee, et al. (2020). For surface measurements, we use version 6.0 of the GLOBALVIEW plus package (Masarie et al., 2014; Cooperative Global Atmospheric Data Integration Project, 2018). For OCO-2 measurements, we use ACOS b10 land (land glint and land nadir) and ocean glint retrievals aggregated into super-obs at $0.5°\times0.5°$ resolution grids following Liu et al. (2017), with the additional requirement that there must be a minimum of three OCO-2 observations within each 0.5°×0.5° grid box per track. We use all data that pass the quality flag filter.

Calculations of the $\Delta X_{CO_2\ top-down}$ signal are performed with the one-way nested grid over Australia. First, we generate boundary conditions by performing a simulation at 2°×2.5° with regrided optimized NEE and ocean fluxes and prescribed fluxes from the 4°×5° flux inversion. Then we run the nested model and sample the OCO-2 and TCCON observations from 1 Oct 2019 through 31 Jan 2020. Finally, we calculate the $\Delta X_{CO_2\ top-down}$ anomaly signal as the data-model mismatch for these simulated observations.

3.3 NEE anomaly estimate

NEE anomalies (ΔNEE) over the 2019–2020 growing season are estimated by combining the constraints on GPP from FluxSat Version 2 (Joiner & Yoshida, 2020) with the constraints on the net CO_2 flux from the top-down $\Delta X_{CO_2\ top-down}$ signal and biomass–burning–$\Delta X_{CO_2\ BB}$. The spatial and temporal structure of ΔNEE is assumed to be directly proportional to ΔGPP from FluxSat, while the magnitude of the ΔNEE is inferred from the atmospheric ΔX_{CO_2} signal.

We calculate ΔGPP from FluxSat as the difference between fluxes for 2019–2020 relative to a 2010-2018 mean. FluxSat estimates GPP based on Nadir BRDF-Adjusted Reflectances (NBAR) from the MODerate-resolution Imaging Spectroradiometer (MODIS) MYD43D product (Schaaf et al., 2002). The GPP estimates are calibrated with the FLUXNET 2015 GPP derived from eddy covariance flux measurements at Tier 1 sites (Joiner & Yoshida, 2020).

Here, NEE is defined as $\mathrm{NEE} = \mathrm{R_{hetero}} - \mathrm{NPP}$, where NPP is net primary production and $\mathrm{R_{hetero}}$ is heterotrophic respiration. Therefore, ΔNEE is due to both anomalies in NPP, where $\mathrm{NPP} \approx 0.5 \times \mathrm{GPP}$ (Waring et al., 1998; DeLucia et al., 2007; Collalti & Prentice, 2019), and $\mathrm{R_{hetero}}$. For this analysis we also assume $\Delta \mathrm{R_{hetero}} \propto \Delta \mathrm{GPP}$, as there are not direct large scale observations that can be related to $\mathrm{R_{hetero}}$. Empirical evidence from the OzFlux eddy covariance network (Li et al., 2017) has found that ΔNEE can be expressed linearly as a function of ΔGPP with reasonable accuracy. Li et al. (2017) find that that $\Delta\mathrm{NEE} = -0.24\,\Delta\mathrm{GPP}$ for non-forest ecosystems, where anomalies in GPP and respiration are correlated, but $\Delta\mathrm{NEE} = -0.8\,\Delta\mathrm{GPP}$ for forest ecosystems, where GPP and respiration do not co-vary.

To estimate the magnitude of ΔNEE, we simulate the OCO-2 observed X_{CO_2} anomaly signal due to ΔGPP ($\Delta X_{CO_2\ GPP}$) using the same approach as was used for biomass burning (See 3.1.1). We invert a magnitude of ΔNEE through regressions of $\Delta X_{CO_2\ NEE}$ against an observationally constrained anomaly in X_{CO_2}:

$$\Delta X_{CO_2\ NEE} + \beta = -\alpha \times \Delta X_{CO_2\ GPP} + \beta = \Delta X_{CO_2\ top-down} - \Delta X_{CO_2\ BB}. \tag{1}$$

Note that β is included to account for possible small residual biases from the observations or model. Initially, we attempted a multivariate regression to solve this for forest and non-forest $\Delta X_{CO_2\ NEE}$ individually but recovered unrealistic negative coefficient for forests. The $\Delta X_{CO_2\ NEE}$ is relatively small and may be impacted by errors in biomass burning emissions and transport, potentially limiting our ability to differentiate forest and non-forest ΔNEE. To avoid these unphysical values, we prescribe the the ratio of ΔNEE between forest and non-forest ecosystems. Following from Li et al. (2017), we perform one regression using

$$\Delta\mathrm{NEE_{total}} \propto -0.24\,\Delta\mathrm{GPP_{non-forest}} - 0.8\,\Delta\mathrm{GPP_{forest}}. \tag{2}$$

However, due to the large CO_2 biomass burning emissions over this event, it is possible that ΔNEE and ΔGPP may diverge from this relationship. Therefore, we also perform a regression using the relationship:

$$\Delta\mathrm{NEE_{total}} \propto -\Delta\mathrm{GPP_{non-forest}} - \Delta\mathrm{GPP_{forest}}. \tag{3}$$

Table 2. Coefficients 'α' obtained by linear regressions that relates ΔNEE and ΔGPP through the relationship $\Delta\text{NEE} = -\alpha\Delta\text{GPP}$. The median and range of α are given for regressions using the eight posterior biomass burning estimates for simulations that vary in the emission height and forest/non-forest parameterization. The bottom row gives the mean and range for the truncated distribution of all simulations, wherin we remove largest and smallest two outliers from the 32 simulations performed by varying biomass burning emissions, emission height, and the forest/non-forest parameterization.

emission height	forest/non-forest parameterization	forest α	non-forest α
		median (range)	median (range)
injection height	$0.24\text{N} + 0.8\text{F}$	0.52 (0.33–1.15)	0.16 (0.10–0.35)
injection height	$\text{N} + \text{F}$	0.26 (0.21-0.42)	0.26 (0.21–0.42)
surface	$0.24\text{N} + 0.8\text{F}$	0.59 (0.42–0.66)	0.18 (0.12–0.20)
surface	$\text{N} + \text{F}$	0.31 (0.23–0.32)	0.31 (0.23–0.32)
		mean (range)	mean (range)
all (truncated)	all (truncated)	0.41 (0.23–0.66)	0.23 (0.13–0.35)

We perform a series of linear regressions using Eq. 1 to estimate 'α', the parameter that relates ΔNEE and ΔGPP. We perform the regression a total of 32 times by varying the emission height of biomass burning emissions between the surface and injection height, the posterior biomass burning emissions estimated by the eight TROPOMI flux inversions, and the parameterization relating forest and non-forest ΔNEE using Eqs 2–3. Table 2 shows the statistics of α for these 32 regressions. The best estimate of α is then calculated a the mean of the truncated distribution of the 32 α values, with the largest and smallest two values removed, and the range of the truncated distribution is taken as the uncertainty. This gives an α of 0.41 (0.23–0.66) for forest ecosystems, which is half the value of Li et al. (2017), and 0.23 (0.13–0.35) for non-forest ecosystem, which is almost identical to the value of Li et al. (2017).

A comparison of the top-down ΔX_{CO_2} and ΔX_{CO_2} simulated by the biomass burning and ΔNEE estimates obtained in this analysis for TCCON and OCO-2 measurements is shown in the supporting information (Fig. S6). We find that the flux estimates found here are generally consistent with these top-down datasets, although there is considerable scatter between different TCCON sites and OCO-2 viewing modes.

4 Carbon cycle anomalies over the 2019–2020 growing season

The climate anomalies over the 2019–2020 growing season can be partitioned into two phases. Warm–dry conditions dominated the region during the austral spring and early summer (October through January), when there were a number of biomass burning events, primarily in the evergreen needleleaf forests (ENFs) and evergreen broadleaf forests (EBFs) along the coast. This was followed by a cooler-wetter period during February through May (Fig. 1a,b). Video 2 [Figure 4/supp Video 2 in pre-print] shows the evolution of ΔNEE and biomass burning over the 2019–2020 growing season. During the warm-dry phase, GPP was suppressed across the region, falling below the range of observed GPP over the 2010–2018 period (2.0 $\text{PgC}\,\text{m}^{-2}\,\text{day}^{-1}$ for Oct-Jan 2019–2020 versus 3.0–4.3 $\text{PgC}\,\text{m}^{-2}\,\text{day}^{-1}$ over 2010–2018). Suppression of productivity occurred uniformly across southeast Australia during Oct-Jan (Fig. 5), impacting both forest and non-forest ecosystems. This is followed by a large-scale recovery in GPP to above average

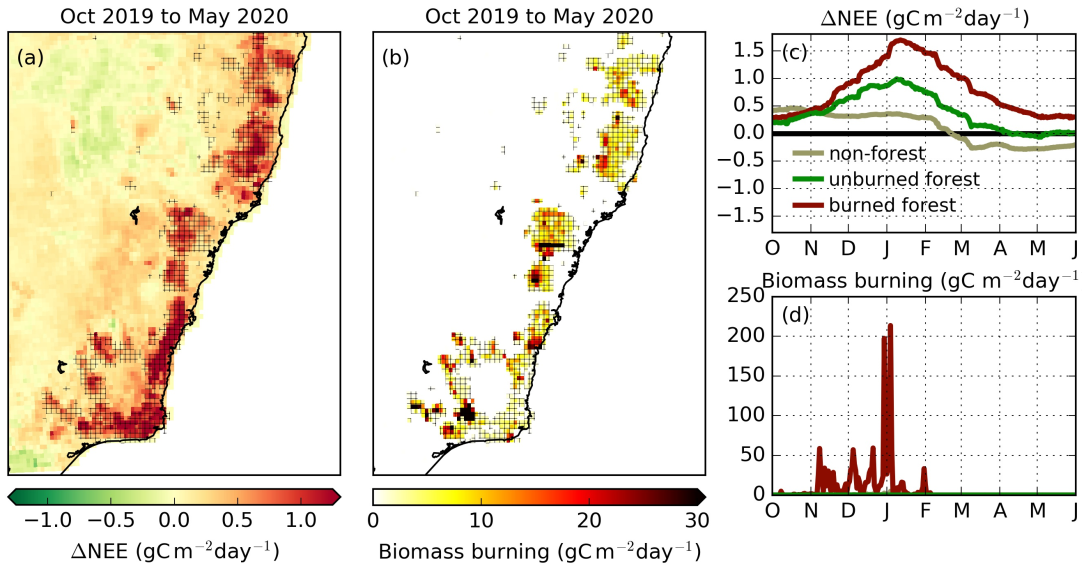

Figure 4. [See Video 2] Daily (a) ΔNEE and (b) biomass burning emissions over southeast Australia. Hatching shows burned area. Timeseries of (c) ΔNEE and (b) biomass burning of for non-forest (light grey), unburned forest (green) and burned forest (red) areas.

values during Feb-May, when cooler-wetter conditions dominate. This recovery was relatively uniform across the region with the exception of burned areas (indicated by hatching in Fig. 5), which show suppression of GPP during Feb-May that is similar to Oct-Jan.

Figure 6 shows the timeseries of ΔGPP for burned and unburned forested regions, as-well as non-forested regions aggregated together (includes cropland, grassland, shurbland, and savanna ecosystems) over southeast Australia (145.5–154.4 E, 28.5–38.5 S). We divide forested regions into burned and unburned regions using a threshold of 50 gC m^{-2} of biomass burning emissions over the 2019–2020 growing season for each 0.1° × 0.1° grid cell. For non-forested regions, GPP was suppressed during Oct–Jan (54% below mean), but rapidly recovered to above average when cooler-wetter conditions dominate (33% above mean for Feb–May). In the unburned forested regions, GPP was suppressed during Oct–Jan (20%/24% below mean for ENF/EBF), with a partial recovery during Feb–May (13%/6% below mean for ENF/EBF). In contrast, the burned forests showed a larger reduction in GPP during Oct–Jan (22%/38% below mean for ENF/EBF) that persisted throughout Feb–May (38/30% below mean for ENF/EBF). Similar reductions are found for MODIS near-infrared reflectance of terrestrial vegetation (NIR_V) and solar induced fluorescence (SIF) measurements from TROPOMI and OCO-2 for these vegetation types (see Text S3. and Figure S6 in the supporting information). These similar results for NIR_V suggest that structural changes in vegetation are partially responsible for the reductions in GPP (He et al., 2020; Sun et al., 2015; Yoshida et al., 2015).

In total, 166 TgC (range: 113–236 TgC) of CO_2 was released through biomass burning and 33 TgC (range: 19–52 TgC) was released due to anomalies in NEE over Oct–May (Table 3). This carbon loss was unevenly spread across vegetation types, with the majority of biomass burning emissions originating from EBFs (71–165 TgC) and ENFs (31–53 TgC). Per unit area, reductions in GPP were more severe in burned forest ecosys-

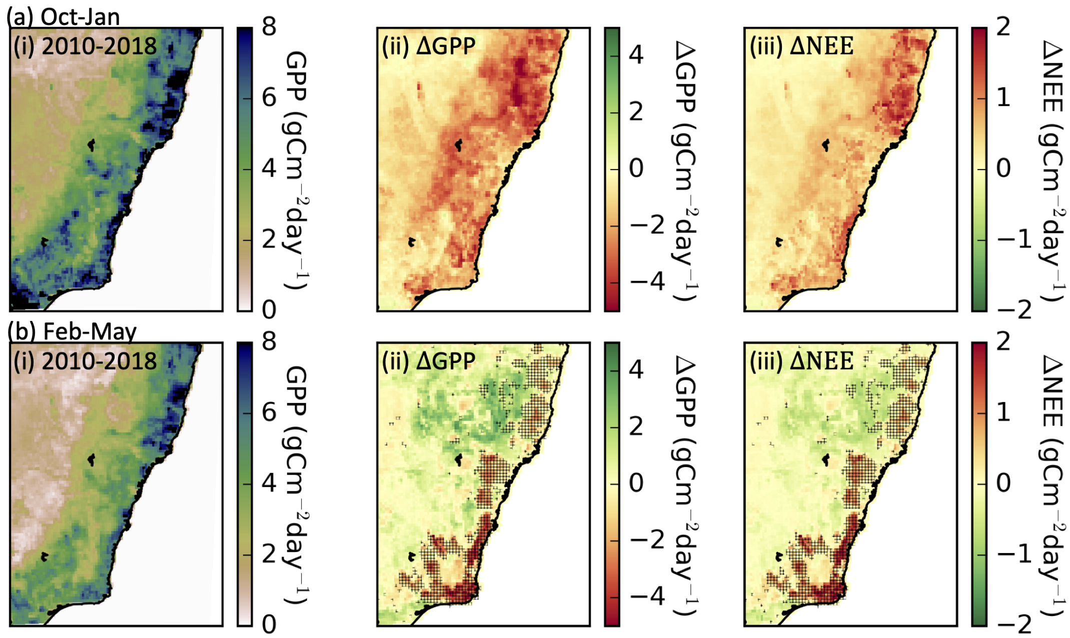

Figure 5. (a) Oct-Jan and (b) Feb-May maps of (i) 2010-2018 mean GPP, (ii) ΔGPP (2019-2020 GPP minus 2010-2018 mean GPP) and (iii) mean estimate of ΔNEE. Hatching shows locations of bushfires during the 2019-2020 growing season.

Table 3. Oct–May net CO_2 fluxes (TgC) due to biomass burning and ΔNEE over southeast Australia.

	non-forest	burned forest	unburned forest	All
BB	20 (18–23)	146 (95–213)	0	166 (112–235)
ΔNEE	12 (7–18)	16 (9–26)	5 (3–8)	33 (19–52)
Total	32 (24–40)	163 (104–239)	5 (3–8)	199 (131–288)

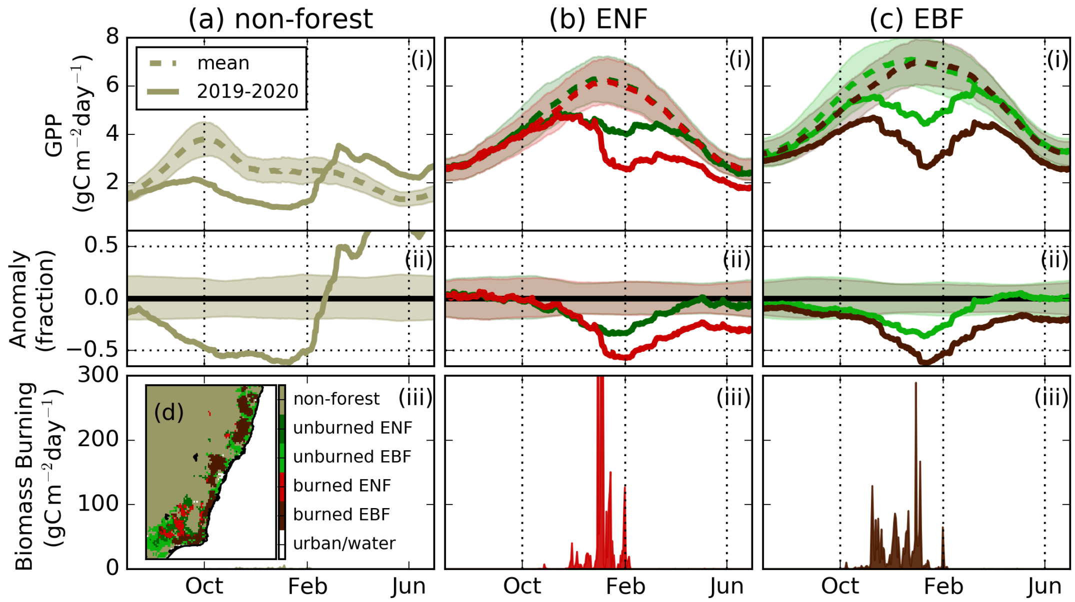

Figure 6. Timeseries of (i) GPP, (ii) anomaly in GPP as a fraction of the mean and (iii) biomass burning emissions for (a) non-forest (combined Cropland/Grassland/Savanna/Shrubland), (b) unburned and burned ENF, and (c) unburned and burned EBF. (d) The spatial extent of non-forest, burned and unburned EBF, and burned and unburned ENF over southeast Australia (145.5–154.4 E, 28.5–38.5 S).

tems. Over Oct–May, reductions in GPP were 1.43 $\mathrm{gC\,m^{-2}\,s^{-1}}$ (29%) for burned ENF, 0.83 $\mathrm{gC\,m^{-2}\,s^{-1}}$ (17%) for unburned ENF, 2.02 $\mathrm{gC\,m^{-2}\,s^{-1}}$ (34%) for burned EBF, 0.94 $\mathrm{gC\,m^{-2}\,s^{-1}}$ (16%) for unburned EBF, and 0.45 $\mathrm{gC\,m^{-2}\,s^{-1}}$ (18%) for non-forest ecosystems.

5 Discussion

5.1 Comparison of biomass burning estimates with other studies

Previous estimates of the 2019–2020 Australian biomass burning emissions have been derived using bottom-up methods. Several estimates are based on burned area, wherein, trace gas emissions are derived from space-based burned area measurements using estimate of fire severity, type of vegetation, mass of fuel and trace gas emission factors. GFED gave CO_2 emissions of 132 TgC for southeast Australia, using a combination of burned area and radiative power observations. The Full Carbon Accounting Model (FullCAM) modelling framework estimated 232 TgC (Australian Government Department of Industry & Resources, 2020) for the Australian temperate zone biomass burning, which was dominated by emissions from southeast Australia but also includes some some small fires in Western Australia and Tasmania. D. M. J. S. Bowman et al. (2020) estimated emissions of 184 TgC (95% confidence interval, 85–282 TgC) for temperate zone biomass burning emissions using a bootstrapping method incorporating potential fuel loads and satellite-based fire severity mapping. In addition to burned area based emission estimates, GFAS provided an estimate of 55 TgC of CO_2 emitted over southeast Australia based on MODIS fire radiative power observations and trace gas emission factors.

A common feature among these existing biomass burning estimates is that the trace gas emissions are modeled based on observations of fire severity and extent. In contrast, the emission estimates calculated in this study are "top-down", in that they are based on observations of the emitted trace gases in the atmosphere. Thus, the differences in approach are complementary, and consistency between top-down and bottom-up estimates provides increased confidence in emission estimates. We obtained a mean estimate of 167 TgC with a range of 113–236 TgC, which overlaps with existing burned-area-based estimates of biomass burning over southeast Australia, providing increased confidence in these estimates. However, our estimated range suggests larger emissions than provided by the GFAS radiative-power-based method, suggesting the GFAS underestimates biomass burning over southeast Australia during 2019–2020.

5.2 Uncertainties in estimating carbon flux

In this analyses, we have calculated drought-induced NEE anomalies and biomass burning CO_2 anomalies over southeast Australia during 2019–2020 that are consistent with observed X_{CO}, X_{CO_2} and FluxSat GPP. Still, there are remaining challenges in quantifying carbon cycle perturbations, leading to large uncertainties in the estimates presented here.

Accurate representation of atmospheric transport of CO and CO_2 from biomass burning remains a major challenge (Eastham & Jacob, 2017). Rapid pyroconvective motions are not well represented in our model simulations. This leads to errors in simulated X_{CO} fields relative to the observations and systematic errors in flux inversions. In our analysis, we performed sensitivity analysis by evaluating the posterior CO fields for emissions released at the surface and at an estimated plume injection height (emitted at up to 6 km in altitude, Text S1 and Figure S1 of the supporting information), and found that the posterior emissions better matched independent CO observations in both cases. Still, Modeled CrIS X_{CO}, which are most sensitive to the upper troposphere, showed weak sensitivity to biomass burning emissions despite the fact that biomass burning species were observed in the stratosphere (Khaykin et al., 2020; Schwartz et al., 2020; Hirsch & Koren, 2021). This suggests that modeled vertical motions are too weak and do not fully capture the vertical structure of biomass burning species produced by strong pyroconvective motions. Such systematic errors are challenging to address, but one possible avenue of future study would be to utilize weak constraint 4D-Var (Stanevich et al., 2019), which would allow for optimizing both surface fluxes and the atmospheric state. Accounting for the total CO change throughout the column would provide a quantitative assessment of the impact of systematic transport errors on CO emission estimates. Another avenue of future work could be to improve the representation of pyroconvective motions in transport models. As these motions are sub-grid scale for typical chemical transport models, this would most likely require prescribing vertical mass fluxes calculated by a high resolution cloud resolving model.

It is also notable that the largest biomass burning enhancements of X_{CO_2} were not observable by OCO-2 or TCCON sites due to the presence of co-emitted aerosols (J. Wang et al., 2020). Rapid deployment of aircraft campaigns that observe the chemical composition of the biomass burning plumes would help mitigate these sampling biases. The serendipitous occurrence of the Atmospheric Carbon and Transport – America (ACT-America) flight campaign during the 2019 Midwest floods provided supporting evidence of the flood-induced CO_2 flux anomalies estimated by Yin et al. (2020), resulting in increased confidence in those estimates.

Finally, we note that we only quantify land-atmosphere CO_2 fluxes in this study, and that a full accounting of the carbon stock changes due to this event would need to incorporate lateral carbon fluxes. Intense rainfall following immediately after fire likely increased runoff of ash and debris to waterways, leading to a number of record fish kills in estuarine sites located downstream of burned areas (Silva et al., 2020). Thus, there may have been considerable export of carbon to waterways and the ocean, but this has not been quantified to our knowledge.

5.3 Implications for southeast Australia

The extensive 2019–2020 fires across EBF and ENF ecosystems were unprecedented in scale and intensity (Abram et al., 2020), but similar events could become more frequent in the future due to climate change (Dowdy et al., 2019; Di Virgilio et al., 2019). This study confirms the large loss of carbon from burned EBF and ENF ecosystems found in previous analyses (D. M. J. S. Bowman et al., 2020; Australian Government Department of Industry & Resources, 2020). In addition to carbon loss through biomass burning, fire-impacted ecosystems continued to show suppressed GPP throughout the austral autumn, suggesting a reduction of growing season carbon uptake. This result is consistent with major structural damages due to biomass burning, which prevent a rapid recovery when favorable conditions return. Previous studies have found that forest ecosystems continue to lose carbon for years after fires (Amiro et al., 2010; Goulden et al., 2011), suggesting that increased fire frequency could severely impact the carbon balance of these ecosystems. Furthermore, frequent fires could limit the ability of forests to recover and lead to structural changes (Fairman et al., 2016) and shifts in species composition (Pellegrini et al., 2021; Fletcher et al., 2014). Overall, this suggests a high sensitivity of forested regions to changes in the frequency of intense fire events.

In unburned ecosystems, drought and heat stress resulted in reduction in GPP of 16-18% over the 2019–2020 austral growing season. This result is consistent with site level observations of foliar death in eucalypt forests during 2019–2020 that were found to be closely associated with hydraulic failure (Nolan et al., 2021), and further supported by $\mathrm{NIR_V}$ and SIF observations (Fig. S6). We find that these reductions in productivity were largely limited to the period with extreme heat and aridity, with no pronounced legacy effects. In fact, GPP quickly recovered to above average productivity for non-forest ecosystems and to average productivity for forest ecosystems. This robust recovery is in contrast with previous studies that have found substantial legacy effects from severe drought, with reduced productivity for years (Anderegg et al., 2015; Wu et al., 2018). For example, Wu et al. (2018) found legacy effects of up to 4 years in forests and up to 2 years in non-forest ecosystems. However, Australian biota are adapted to high-temperature and water-limited conditions, which may make them well placed for rapid recovery of GPP given some rainfall (Saadaoui et al., 2017; Haverd et al., 2017; Beadle & Sands, 2004; Arndt et al., 2015). Thus, the results of this study suggest a rapid recovery for unburned ecosystems, and indicate that these ecosystems may not experience strong legacy effects to heat and drought events. However, given that we only examine the carbon balance for a single growing season, it is unclear if the drought and heat impacted ecosystems could show longer-term legacy effects during future years. Furthermore, the robust recovery from this event may be unusual, as it ended abruptly with heavy rainfall and below average temperatures. The timing and magnitude of rainfall is very important in the response of dryland ecosystems to rain (Huxman et al., 2004; Haverd et al., 2017). Finally, we note that this analysis only addresses space-based GPP estimates; previous analysis has shown long-term changes in canopy structure (Saatchi et al., 2013) following extreme drought, which may not be detected in this analysis. Similarly, there could be undetected changes in species composition. We recommend future analysis that look at the longer-term response to this event.

6 Conclusions

Extreme events play a major role in the carbon cycling of ecosystems, but quantifying the impact of these events on the carbon budget remains challenging. Incorporating a variety of space-based observations, we have provided a comprehensive accounting of biosphere-atmosphere CO_2 flux anomalies due to drought, heat, and fire over southeast Australia (145.5–154.4 E, 28.5–38.5 S) during the 2019-2020 austral growing season. In total, biomass burning released 113–236 TgC of CO_2 and anomalies in Oct–May NEE reduced carbon uptake by 19–52 TgC. Carbon losses were found to be most severe in forested regions and were dominated by biomass burning emissions. Unburned forests and non-forest ecosystems recovered to mean or greater productivity when cooler-wetter conditions dominated during the late austral summer and autumn, however, primary productivity remained suppressed in burned regions.

This analysis finds that space-based remote sensing of trace gases and MODIS reflectances provide strong constraints on carbon cycle anomalies produced by extreme events. Still, there are remaining challenges that result in significant uncertainties in inferred fluxes. For inferring biomass burning estimates from X_{CO} measurements, resolving pyroconvective tracer transport remains a major challenge and source of uncertainty. In addition, aerosols co-emitted with biomass burning CO and CO_2 prevent trace gas measurements within much of the biomass burning plume. Furthermore, estimates of NEE anomalies based on GPP anomalies require assumptions about anomalies in heterotrophic respiration that were uncertain and overly simplistic.

The frequency of extreme heat and fire events have increased in southeast Australia (Abram et al., 2020; Sharples et al., 2016), a trend that is expected to continue with climate change (Perkins-Kirkpatrick & Gibson, 2017; Abatzoglou et al., 2019), including increased risk of more intense pyroconvective fires (Dowdy et al., 2019; Di Virgilio et al., 2019). The large fire-induced carbon loss reported here, coupled with evidence of slow (> 10 years) recovery from major fires (Amiro et al., 2010; Goulden et al., 2011; Fairman et al., 2016), suggests that the carbon sink in southeast Australia could be sensitive to increased fire frequency.

Appendix A Flux inversion configuration

The nested CO flux inversions are performed over a one-way nested domain of ($100^\circ-177.5^\circ$ E, $0^\circ - 60^\circ$ S) at $0.5^\circ\times0.625^\circ$ spatial resolution. Assimilated TROPOMI X_{CO} super-obs are generated by aggregating measurements with the quality flag $\geq$0.5 to the $0.5^\circ\times0.625^\circ$ spatial grid. The flux inversions optimize scaling factors to each model gridcell for prior biomass burning emissions from 5 Nov 2019 through 14 Jan 2020. Prior biomass burning emissions vary between flux inversions and are listed in Table 1. For the anthropogenic emissions, we combine off-line emission inventories from the EDGAR 4.2 global model (Olivier & Berdowski, 2001) and several regional models including the US Environmental Protection Agency (EPA) National Emission Inventory (NEI) for 2008 in North America, the Criteria Air Contaminants (CAC) inventory for Canada, the Big Bend Regional Aerosol and Visibility Observational (BRAVO) Study Emissions Inventory for Mexico (Kuhns et al., 2003),the Cooperative Program for Monitoring and Evaluation of the Long-range Transmission of Air Pollutants in Europe (EMEP) inventory for Europe in 2000 (Vestreng, 2002) and the Streets Asia emissions inventory for 2000 (Streets et al., 2006). Monthly BioFuel emissions are from the Emission Database for Global Atmospheric Research (EDGAR) (Crippa et al., 2016), monthly shipping emissions from the International Comprehensive Ocean–Atmosphere Data Set (ICOADS) (C. Wang et al., 2008), and hourly Biogenic emissions from Model of Emissions of Gases and Aerosols from Nature (MEGAN) (Guenther et al., 2012).

Boundary conditions for the nested flux inversions are generated by performing a global inversion with GHGF-Flux at $4^\circ\times5^\circ$ spatial resolution over the three month period from November 2019 through January 2020. The global inversion assimilates TROPOMI X_{CO} super-obs (aggregated to $4^\circ\times5^\circ$ for measurements with quality flag equal to one) to optimize 14-day scale factors for prior GFED biomass burning emissions at each grid cell. Other prescribed emissions are identical to the nested flux inversion. Initial conditions for the global flux inversion are obtained from a global MOPITT X_{CO} flux inversion. To test the sensitivity of inferred fluxes to the boundary conditions on the nested flux inversions, we generate a second set of boundary conditions that are identical to those from the global TROPOMI flux inversion but have CO increased by 10 ppb at all times and locations.

Acknowledgments

BB was supported by an appointment to the NASA Postdoctoral Program at the Jet Propulsion Laboratory, administered by Universities Space Research Association under contract with NASA. BB and JL were supported by the NASA OCO2/3 science team program NNH17ZDA001N-OCO2. KWB was supported by the NASA Carbon Monitoring System (CMS) project (NNH16ZDA001N-CMS). JJ was supported by the NASA Making Earth System Data Records for Use in Research Environments (MEaSUREs) and Arctic Boreal Vulnerability Experiment (ABoVE) programs. The research carried out at the Jet Propulsion Laboratory, California Institute of Technology, was under a contract with the National Aeronautics and Space Administration. Resources supporting this work were provided by the NASA High-End Computing (HEC) Program through the NASA Advanced Supercomputing (NAS) Division at Ames Research Center. ODIAC project is supported by Greenhouse Gas Observing SATellite (GOSAT) project, National Institute for Environmental Studies (NIES), Japan.

GFED data were downloaded from https://www.globalfiredata.org/. GFAS data were downloaded from https://apps.ecmwf.int/datasets/. GFAS is generated using Copernicus Atmosphere Monitoring Service Information 2020, neither the European Commission nor ECMWF is responsible for any use that may be made of the information it contains. TCCON data were obtained from the TCCON Data Archive, hosted by CaltechDATA (https://tccondata.org). Wollongong TCCON measurements over the period of this study are supported by the Australian Research Council (ARC) grants DP160101598 and LE0668470, while NMD is supported by an ARC Future Fellowship, FT180100327. We downloaded version 9 of the ACOS OCO-2 lite files from the CO_2 Virtual Science Data Environment (https://CO_2.jpl.nasa.gov/). OCO-2 data were produced by the OCO-2 project at the Jet Propulsion Laboratory, California Institute of Technology, and obtained from the OCO-2 data archive maintained at the NASA Goddard Earth Science Data and Information Services Center. FluxSat data were downloaded from https://avdc.gsfc.nasa.gov/pub/tmp/ MODIS land cover data was downloaded from the EOSDIS Land Processes DAAC. ETOPO1 elevation data was downloaded from https://www.ngdc.noaa.gov. ERA5-Land data are obtained from the Climate Data Store (https://cds.climate.copernicus.eu). TROPOMI CO data were downloaded from http://www.tropomi.eu/data-products/carbon-monoxide. CrIS CO is provided by the NASA TRoposperhic Ozone and its Precursors from Earth System Sounding (TROPESS) and available from https://tes.jpl.nasa.gov. MODIS NIRv was calculated from MODIS NBAR measurements (MCD43A4), which were downloaded from the LP DAAC. TROPOMI L2 SIF data were downloaded from ftp://fluo.gps.caltech.edu/data/tropomi/ung OCO-2 L2 SIF data are available from the GES DISC (https://disc.gsfc.nasa.gov). The grided daily estimates of ΔNEE and biomass burning will be made publicly available upon publication.

References

Abatzoglou, J. T., Williams, A. P., & Barbero, R. (2019). Global emergence of anthropogenic climate change in fire weather indices. *Geophysical Research Letters*, *46*(1), 326–336.

Abram, N. J., Henley, B. J., Gupta, A. S., Lippmann, T. J., Clarke, H., Dowdy,

A. J., ... others (2020). Connections of climate change and variability to large and extreme forest fires in southeast Australia. *Communications Earth & Environment*, *2*(1), 1–17.

Akagi, S. K., Yokelson, R. J., Wiedinmyer, C., Alvarado, M. J., Reid, J. S., Karl, T., ... Wennberg, P. O. (2011). Emission factors for open and domestic biomass burning for use in atmospheric models. *Atmospheric Chemistry and Physics*, *11*(9), 4039–4072. Retrieved from `https://acp.copernicus.org/articles/11/4039/2011/` doi: 10.5194/acp-11-4039-2011

Amante, C., & Eakins, B. W. (2009). ETOPO1 arc-minute global relief model: procedures, data sources and analysis.

Amiro, B. D., Barr, A. G., Barr, J., Black, T. A., Bracho, R., Brown, M., ... others (2010). Ecosystem carbon dioxide fluxes after disturbance in forests of North America. *Journal of Geophysical Research: Biogeosciences*, *115*(G4).

Anderegg, W. R., Schwalm, C., Biondi, F., Camarero, J. J., Koch, G., Litvak, M., ... others (2015). Pervasive drought legacies in forest ecosystems and their implications for carbon cycle models. *Science*, *349*(6247), 528–532.

Arndt, S. K., Sanders, G. J., Bristow, M., Hutley, L. B., Beringer, J., & Livesley, S. J. (2015). Vulnerability of native savanna trees and exotic khaya senegalensis to seasonal drought. *Tree physiology*, *35*(7), 783–791. doi: 10.1093/treephys/tpv037

Australian Government Department of Industry, E., Science, & Resources. (2020). *Estimating greenhouse gas emissions from bushfires in Australia's temperate forests: focus on 2019–20.* Retrieved from `https://www.industry.gov.au/sites/default/files/2020-04/estimating-greenhouse-gas-emissions-from-bushfires-in-australias-temperate-forests-focus-on-2019-20.pdf`

Bastos, A., Gouveia, C., Trigo, R., & Running, S. W. (2014). Analysing the spatio-temporal impacts of the 2003 and 2010 extreme heatwaves on plant productivity in europe. *Biogeosciences*, 3421–3435.

Beadle, C., & Sands, P. (2004). Synthesis of the physiological, environmental, genetic and silvicultural determinants of the growth and productivity of eucalypts in plantations. *Forest ecology and management*. doi: 10.1016/j.foreco.2004.01.026

Boer, M. M., de Dios, V. R., & Bradstock, R. A. (2020). Unprecedented burn area of Australian mega forest fires. *Nature Climate Change*, *10*(3), 171–172.

Borsdorff, T., Aan de Brugh, J., Hu, H., Aben, I., Hasekamp, O., & Landgraf, J. (2018). Measuring carbon monoxide with TROPOMI: First results and a comparison with ECMWF-IFS analysis data. *Geophysical Research Letters*, *45*(6), 2826–2832.

Bowman, D. M. J. S., Balch, J. K., Artaxo, P., Bond, W. J., Carlson, J. M., Cochrane, M. A., ... others (2009). Fire in the earth system. *science*, *324*(5926), 481–484.

Bowman, D. M. J. S., Williamson, G. J., Price, O. F., Ndalila, M. N., & Bradstock, R. A. (2020). Australian forests, megafires and the risk of dwindling carbon stocks. *Plant, Cell & Environment*.

Bowman, K. W., Rodgers, C. D., Kulawik, S. S., Worden, J., Sarkissian, E., Osterman, G., ... others (2006). Tropospheric emission spectrometer: Retrieval method and error analysis. *IEEE Transactions on Geoscience and Remote Sensing*, *44*(5), 1297–1307.

Bureau of Meteorology. (2020). *Annual climate statement 2019.* Retrieved from `http://www.bom.gov.au/climate/current/annual/aus/#tabs=Overview`

Byrne, B., Liu, J., Bloom, A. A., Bowman, K. W., Butterfield, Z., Joiner, J., ... Yin, Y. (2020). Contrasting regional carbon cycle responses to seasonal climate anomalies across the east-west divide of temperate north america. *Global Biogeochemical Cycles*, e2020GB006598.

Byrne, B., Liu, J., Lee, M., Baker, I. T., Bowman, K. W., Deutscher, N. M., ... Wunch, D. (2020). Improved constraints on northern extratropical CO_2 fluxes obtained by combining surface-based and space-based atmospheric CO_2 measurements. *Journal of Geophysical Research: Atmospheres*, *125*. doi: 10.1029/2019JD032029

Ciais, P., Reichstein, M., Viovy, N., Granier, A., Ogée, J., Allard, V., ... others (2005). Europe-wide reduction in primary productivity caused by the heat and drought in 2003. *Nature*, *437*(7058), 529–533. doi: https://doi.org/10.1038/nature03972

Collalti, A., & Prentice, I. C. (2019, 05). Is NPP proportional to GPP? Waring's hypothesis 20 years on. *Tree Physiology*, *39*(8), 1473-1483. Retrieved from https://doi.org/10.1093/treephys/tpz034 doi: 10.1093/treephys/tpz034

Collins, L., Bradstock, R. A., Clarke, H., Clarke, M. F., Nolan, R. H., & Penman, T. D. (2021). The 2019/2020 mega-fires exposed Australian ecosystems to an unprecedented extent of high-severity fire. *Environmental Research Letters*, *16*(4), 044029.

Cooperative Global Atmospheric Data Integration Project. (2018). *Multi-laboratory compilation of atmospheric carbon dioxide data for the period 1957-2017; obspack_CO_2_1_globalviewplus_v4.1_2018_10_29; noaa earth system research laboratory, global monitoring division.* doi: 10.25925/20181026

Crippa, M., Janssens-Maenhout, G., Dentener, F., Guizzardi, D., Sindelarova, K., Muntean, M., ... Granier, C. (2016). Forty years of improvements in european air quality: regional policy-industry interactions with global impacts. *Atmospheric Chemistry and Physics*, *16*(6), 3825–3841.

Crisp, D., Fisher, B. M., O'Dell, C., Frankenberg, C., Basilio, R., Bösch, H., ... Yung, Y. L. (2012). The ACOS CO_2 retrieval algorithm-Part II: Global XCO_2 data characterization. *Atmos. Meas. Tech.*, *5*(4), 687–707. Retrieved from http://www.atmos-meas-tech.net/5/687/2012/ doi: 10.5194/amt-5-687-2012

Deb, P., Moradkhani, H., Abbaszadeh, P., Kiem, A. S., Engström, J., Keellings, D., & Sharma, A. (2020). Causes of the widespread 2019–2020 Australian bushfire season. *Earth's Future*, e2020EF001671.

De Boeck, H. J., Dreesen, F. E., Janssens, I. A., & Nijs, I. (2011). Whole-system responses of experimental plant communities to climate extremes imposed in different seasons. *New Phytologist*, *189*(3), 806–817.

DeLucia, E. H., Drake, J. E., Thomas, R. B., & Gonzalez-Meler, M. (2007). Forest carbon use efficiency: is respiration a constant fraction of gross primary production? *Global Change Biology*, *13*(6), 1157–1167.

Denton, E. M., Dietrich, J. D., Smith, M. D., & Knapp, A. K. (2017). Drought timing differentially affects above-and belowground productivity in a mesic grassland. *Plant Ecology*, *218*(3), 317–328.

Di Giuseppe, F., Rémy, S., Pappenberger, F., & Wetterhall, F. (2018). Using the Fire Weather Index (FWI) to improve the estimation of fire emissions from fire radiative power (FRP) observations. *Atmospheric Chemistry and Physics*, *18*(8), 5359–5370. Retrieved from https://acp.copernicus.org/articles/18/5359/2018/ doi: 10.5194/acp-18-5359-2018

Di Virgilio, G., Evans, J. P., Blake, S. A., Armstrong, M., Dowdy, A. J., Sharples, J., & McRae, R. (2019). Climate change increases the potential for extreme wildfires. *Geophysical Research Letters*, *46*(14), 8517–8526.

Dowdy, A. J., Ye, H., Pepler, A., Thatcher, M., Osbrough, S. L., Evans, J. P., ... McCarthy, N. (2019). Future changes in extreme weather and pyroconvection risk factors for Australian wildfires. *Scientific reports*, *9*(1), 1–11.

Eastham, S. D., & Jacob, D. J. (2017). Limits on the ability of global eulerian models to resolve intercontinental transport of chemical plumes. *Atmospheric Chemistry and Physics*, *17*(4), 2543–2553. Retrieved from https://acp.copernicus.org/articles/17/2543/2017/ doi: 10.5194/acp-17-2543-2017

Fairman, T. A., Nitschke, C. R., & Bennett, L. T. (2016). Too much, too soon? a review of the effects of increasing wildfire frequency on tree mortality and regeneration in temperate eucalypt forests. *International Journal of Wildland Fire*, *25*(8), 831–848.

Fletcher, M.-S., Wood, S. W., & Haberle, S. G. (2014). A fire-driven shift from forest to non-forest: evidence for alternative stable states? *Ecology*, *95*(9), 2504–2513.

Frank, D., Reichstein, M., Bahn, M., Thonicke, K., Frank, D., Mahecha, M. D., … others (2015). Effects of climate extremes on the terrestrial carbon cycle: concepts, processes and potential future impacts. *Global change biology*, *21*(8), 2861–2880.

Friedl, M., & Sulla-Menashe, D. (2015). MCD12C1 MODIS/Terra+ Aqua Land Cover Type Yearly L3 Global 0.05 Deg CMG V006 [Data set]. *NASA EOSDIS Land Processes DAAC*.

Fu, D., Bowman, K. W., Worden, H. M., Natraj, V., Worden, J. R., Yu, S., … Han, Y. (2016). High-resolution tropospheric carbon monoxide profiles retrieved from CrIS and TROPOMI. *Atmospheric Measurement Techniques*, *9*(6), 2567–2579. Retrieved from https://amt.copernicus.org/articles/9/2567/2016/ doi: 10.5194/amt-9-2567-2016

Gelaro, R., McCarty, W., Suárez, M. J., Todling, R., Molod, A., Takacs, L., … others (2017). The modern-era retrospective analysis for research and applications, version 2 (MERRA-2). *J. Climate*, *30*(14), 5419–5454.

Giglio, L., Randerson, J. T., & Van Der Werf, G. R. (2013). Analysis of daily, monthly, and annual burned area using the fourth-generation global fire emissions database (gfed4). *Journal of Geophysical Research: Biogeosciences*, *118*(1), 317–328.

Goulden, M. L., McMillan, A., Winston, G., Rocha, A., Manies, K., Harden, J. W., & Bond-Lamberty, B. (2011). Patterns of NPP, GPP, respiration, and NEP during boreal forest succession. *Global Change Biology*, *17*(2), 855–871.

Griffith, D. W., Velazco, V. A., Deutscher, N. M., Paton-Walsh, C., Jones, N. B., Wilson, S. R., … Riggenbach, M. O. (2014). *TCCON data from Wollongong (AU), Release GGG2014.R0.* CaltechDATA. Retrieved from https://data.caltech.edu/records/291 doi: 10.14291/tccon.ggg2014.wollongong01.r0/1149291

Guenther, A. B., Jiang, X., Heald, C. L., Sakulyanontvittaya, T., Duhl, T., Emmons, L. K., & Wang, X. (2012). The model of emissions of gases and aerosols from nature version 2.1 (megan2.1): an extended and updated framework for modeling biogenic emissions. *Geoscientific Model Development*, *5*(6), 1471–1492. Retrieved from https://gmd.copernicus.org/articles/5/1471/2012/ doi: 10.5194/gmd-5-1471-2012

Harris, S., & Lucas, C. (2019). Understanding the variability of Australian fire weather between 1973 and 2017. *PloS one*, *14*(9), e0222328.

Haverd, V., Ahlström, A., Smith, B., & Canadell, J. G. (2017). Carbon cycle responses of semi-arid ecosystems to positive asymmetry in rainfall. *Global change biology*, *23*(2), 793–800. doi: 10.1111/gcb.13412

He, L., Wood, J. D., Sun, Y., Magney, T., Dutta, D., Köhler, P., … Frankenberg, C. (2020). Tracking seasonal and interannual variability in photosynthetic downregulation in response to water stress at a temperate deciduous forest. *Journal of Geophysical Research: Biogeosciences*, *125*(8), e2018JG005002.

Henze, D. K., Hakami, A., & Seinfeld, J. H. (2007). Development of the adjoint of GEOS-Chem. *Atmos. Chem. Phys.*, *7*(9), 2413–2433.

Hirsch, E., & Koren, I. (2021). Record-breaking aerosol levels explained by smoke injection into the stratosphere. *Science*, *371*(6535), 1269–1274.

Huxman, T. E., Snyder, K. A., Tissue, D., Leffler, A. J., Ogle, K., Pockman, W. T., … Schwinning, S. (2004). Precipitation pulses and carbon fluxes in semiarid and arid ecosystems. *Oecologia*, *141*(2), 254–268.

Joiner, J., & Yoshida, Y. (2020). Satellite-based reflectances capture large fraction of variability in global gross primary production (GPP) at weekly time scales. *Agricultural and Forest Meteorology*, *291*, 108092.

Kaiser, J. W., Heil, A., Andreae, M. O., Benedetti, A., Chubarova, N., Jones, L., … van der Werf, G. R. (2012). Biomass burning emissions estimated with a global fire assimilation system based on observed fire radiative power. *Biogeosciences*, *9*(1), 527–554. Retrieved from `https://bg.copernicus.org/articles/9/527/2012/` doi: 10.5194/bg-9-527-2012

Khaykin, S., Legras, B., Bucci, S., Sellitto, P., Isaksen, L., Tence, F., … others (2020). The 2019/20 Australian wildfires generated a persistent smoke-charged vortex rising up to 35 km altitude. *Communications Earth & Environment*, *1*(1), 1–12.

King, A. D., Pitman, A. J., Henley, B. J., Ukkola, A. M., & Brown, J. R. (2020). The role of climate variability in Australian drought. *Nature Climate Change*, *10*(3), 177–179.

Kuhns, H., Green, M., Etyemezian, V., Watson, J., & Pitchford, M. (2003). Big bend regional aerosol and visibility observational (BRAVO) study emissions inventory. *Report prepared for BRAVO Steering Committee, Desert Research Institute, Las Vegas, Nevada*.

Landgraf, J., aan de Brugh, J., Scheepmaker, R., Borsdorff, T., Hu, H., Houweling, S., … Hasekamp, O. (2016). Carbon monoxide total column retrievals from TROPOMI shortwave infrared measurements. *Atmospheric Measurement Techniques*, *9*(10), 4955–4975. Retrieved from `https://amt.copernicus.org/articles/9/4955/2016/` doi: 10.5194/amt-9-4955-2016

Li, L., Wang, Y.-P., Beringer, J., Shi, H., Cleverly, J., Cheng, L., … others (2017). Responses of LAI to rainfall explain contrasting sensitivities to carbon uptake between forest and non-forest ecosystems in Australia. *Scientific reports*, *7*(1), 1–9.

Liu, J., Bowman, K. W., Lee, M., Henze, D. K., Bousserez, N., Brix, H., … others (2014). Carbon monitoring system flux estimation and attribution: impact of ACOS-GOSAT XCO_2 sampling on the inference of terrestrial biospheric sources and sinks. *Tellus B*, *66*(1), 22486. doi: 10.3402/tellusb.v66.22486

Liu, J., Bowman, K. W., Schimel, D. S., Parazoo, N. C., Jiang, Z., Lee, M., … Eldering, A. (2017). Contrasting carbon cycle responses of the tropical continents to the 2015–2016 El Niño. *Science*, *358*(6360). Retrieved from `http://science.sciencemag.org/content/358/6360/eaam5690` doi: 10.1126/science.aam5690

Longo, M., Saatchi, S., Keller, M., Bowman, K., Ferraz, A., Moorcroft, P. R., … others (2020). Impacts of degradation on water, energy, and carbon cycling of the Amazon tropical forests. *Journal of Geophysical Research: Biogeosciences*, *125*(8), e2020JG005677.

Masarie, K., Peters, W., Jacobson, A., & Tans, P. (2014). Obspack: a framework for the preparation, delivery, and attribution of atmospheric greenhouse gas measurements. *Earth Syst. Sci. Data*, *6*(2), 375–384.

Mu, M., Randerson, J., Van der Werf, G., Giglio, L., Kasibhatla, P., Morton, D., … others (2011). Daily and 3-hourly variability in global fire emissions and consequences for atmospheric model predictions of carbon monoxide. *Journal of Geophysical Research: Atmospheres*, *116*(D24).

Munoz Sabater, J. (2019). *Copernicus Climate Change Service (C3S) Climate Data Store (CDS).* (2020-08-11) doi: 10.24381/cds.68d2bb30

Nolan, R. H., Boer, M. M., Collins, L., Resco de Dios, V., Clarke, H., Jenkins, M., … Bradstock, R. A. (2020). Causes and consequences of eastern Australia's

2019–20 season of mega-fires. *Global change biology*, *26*(3), 1039–1041.

Nolan, R. H., Gauthey, A., Losso, A., Medlyn, B. E., Smith, R., Chhajed, S. S., ... others (2021). Hydraulic failure and tree size linked with canopy die-back in eucalypt forest during extreme drought. *New Phytologist*.

O'Dell, C. W., Connor, B., Bösch, H., O'Brien, D., Frankenberg, C., Castano, R., ... Wunch, D. (2012). The ACOS CO_2 retrieval algorithm – part 1: Description and validation against synthetic observations. *Atmos. Meas. Tech.*, *5*(1), 99–121. Retrieved from `http://www.atmos-meas-tech.net/5/99/2012/` doi: 10.5194/amt-5-99-2012

Olivier, J., & Berdowski, J. (2001). Global emissions sources and sinks. the climate system. *Lisse, The Netherlands: AA Balkema Publishers/Swets & Zeitlinger Publishers90*, *5809*(255), 0.

Pellegrini, A. F., Refsland, T., Averill, C., Terrer, C., Staver, A. C., Brockway, D. G., ... others (2021). Decadal changes in fire frequencies shift tree communities and functional traits. *Nature Ecology & Evolution*, *5*(4), 504–512.

Perkins-Kirkpatrick, S., & Gibson, P. (2017). Changes in regional heatwave characteristics as a function of increasing global temperature. *Scientific Reports*, *7*(1), 1–12.

Pollard, D. F., Robinson, J., & Shiona., H. (2019). *TCCON data from Lauder, New Zealand, 125HR, release GGG2014R0.* CaltechDATA. doi: 10.14291/tccon.ggg2014.lauder03.R0

Pollard, D. F., Sherlock, V., Robinson, J., Deutscher, N. M., Connor, B., & Shiona, H. (2017). The Total Carbon Column Observing Network site description for Lauder, New Zealand. *Earth System Science Data*, *9*(2), 977–992. Retrieved from `https://essd.copernicus.org/articles/9/977/2017/` doi: 10.5194/essd-9-977-2017

Randerson, J. T., Chen, Y., Van Der Werf, G., Rogers, B., & Morton, D. (2012). Global burned area and biomass burning emissions from small fires. *Journal of Geophysical Research: Biogeosciences*, *117*(G4).

Reichstein, M., Ciais, P., Papale, D., Valentini, R., Running, S., Viovy, N., ... others (2007). Reduction of ecosystem productivity and respiration during the european summer 2003 climate anomaly: a joint flux tower, remote sensing and modelling analysis. *Global Change Biology*, *13*(3), 634–651.

Rémy, S., Veira, A., Paugam, R., Sofiev, M., Kaiser, J. W., Marenco, F., ... Hair, J. W. (2017). Two global data sets of daily fire emission injection heights since 2003. *Atmospheric Chemistry and Physics*, *17*(4), 2921–2942. Retrieved from `https://acp.copernicus.org/articles/17/2921/2017/` doi: 10.5194/acp-17-2921-2017

Saadaoui, E., Yahia, K. B., Dhahri, S., Jamaa, M. L. B., & Khouja, M. L. (2017). An overview of adaptative responses to drought stress in eucalyptus spp. *Forestry Studies*, *67*(1), 86–96. doi: 10.1515/fsmu-2017-0014

Saatchi, S., Asefi-Najafabady, S., Malhi, Y., Aragão, L. E., Anderson, L. O., Myneni, R. B., & Nemani, R. (2013). Persistent effects of a severe drought on Amazonian forest canopy. *Proceedings of the National Academy of Sciences*, *110*(2), 565–570.

Schaaf, C. B., Gao, F., Strahler, A. H., Lucht, W., Li, X., Tsang, T., ... others (2002). First operational BRDF, albedo nadir reflectance products from MODIS. *Remote sensing of Environment*, *83*(1-2), 135–148.

Schwartz, M. J., Santee, M. L., Pumphrey, H. C., Manney, G. L., Lambert, A., Livesey, N. J., ... Werner, F. (2020). Australian New Year's PyroCb impact on stratospheric composition. *Geophysical Research Letters*, *47*(24), e2020GL090831.

Sharples, J. J., Cary, G. J., Fox-Hughes, P., Mooney, S., Evans, J. P., Fletcher, M.-S., ... Baker, P. (2016). Natural hazards in Australia: extreme bushfire. *Climatic Change*, *139*(1), 85–99.

Silva, L. G., Doyle, K. E., Duffy, D., Humphries, P., Horta, A., & Baumgartner, L. J. (2020). Mortality events resulting from australia's catastrophic fires threaten aquatic biota. *Global Change Biology*, *26*(10), 5345–5350.

Sippel, S., Reichstein, M., Ma, X., Mahecha, M. D., Lange, H., Flach, M., & Frank, D. (2018). Drought, heat, and the carbon cycle: a review. *Current Climate Change Reports*, 1–21.

Stanevich, I., Jones, D. B. A., Strong, K., Keller, M., Henze, D. K., Parker, R. J., ... Deng, F. (2019). Characterizing model errors in chemical transport modelling of methane: Using GOSAT X_{CH_4} data with weak constraint four-dimensional variational data assimilation. *Atmospheric Chemistry and Physics Discussions*, *2019*, 1–54. Retrieved from https://acp.copernicus.org/preprints/acp-2019-786/ doi: 10.5194/acp-2019-786

Streets, D. G., Zhang, Q., Wang, L., He, K., Hao, J., Wu, Y., ... Carmichael, G. R. (2006). Revisiting China's CO emissions after the transport and chemical evolution over the pacific (TRACE-P) mission: Synthesis of inventories, atmospheric modeling, and observations. *Journal of Geophysical Research: Atmospheres*, *111*(D14).

Sun, Y., Fu, R., Dickinson, R., Joiner, J., Frankenberg, C., Gu, L., ... Fernando, N. (2015). Drought onset mechanisms revealed by satellite solar-induced chlorophyll fluorescence: Insights from two contrasting extreme events. *Journal of Geophysical Research: Biogeosciences*, *120*(11), 2427–2440.

Turner, A. J., Köhler, P., Magney, T. S., Frankenberg, C., Fung, I., & Cohen, R. C. (2020). A double peak in the seasonality of california's photosynthesis as observed from space. *Biogeosciences*, *17*(2), 405–422. Retrieved from https://bg.copernicus.org/articles/17/405/2020/ doi: 10.5194/bg-17-405-2020

van der Werf, G. R., Randerson, J. T., Giglio, L., van Leeuwen, T. T., Chen, Y., Rogers, B. M., ... Kasibhatla, P. S. (2017). Global fire emissions estimates during 1997–2016. *Earth Syst. Sci. Data*, *9*(2), 697–720. Retrieved from https://www.earth-syst-sci-data.net/9/697/2017/ doi: 10.5194/essd-9-697-2017

Veefkind, J., Aben, I., McMullan, K., Förster, H., De Vries, J., Otter, G., ... others (2012). TROPOMI on the ESA Sentinel-5 Precursor: A GMES mission for global observations of the atmospheric composition for climate, air quality and ozone layer applications. *Remote sensing of environment*, *120*, 70–83.

Vestreng, V. (2002). Emission data reported to UNECE/EMEP: Quality assurance and trend analysis & presentation of WebDab: MSC-W status report 2002.

Wang, C., Corbett, J. J., & Firestone, J. (2008). Improving spatial representation of global ship emissions inventories. *Environmental Science & Technology*, *42*(1), 193–199.

Wang, J., Liu, Z., Zeng, N., Jiang, F., Wang, H., & Ju, W. (2020). Spaceborne detection of X_{CO_2} enhancement induced by Australian mega-bushfires. *Environmental Research Letters*, *15*(12), 124069.

Ward, M., Tulloch, A. I., Radford, J. Q., Williams, B. A., Reside, A. E., Macdonald, S. L., ... others (2020). Impact of 2019–2020 mega-fires on Australian fauna habitat. *Nature Ecology & Evolution*, *4*(10), 1321–1326.

Waring, R., Landsberg, J., & Williams, M. (1998). Net primary production of forests: a constant fraction of gross primary production? *Tree physiology*, *18*(2), 129–134.

Wu, X., Liu, H., Li, X., Ciais, P., Babst, F., Guo, W., ... others (2018). Differentiating drought legacy effects on vegetation growth over the temperate northern hemisphere. *Global change biology*, *24*(1), 504–516.

Wunch, D., Toon, G. C., Blavier, J.-F. L., Washenfelder, R. A., Notholt, J., Connor, B. J., ... Wennberg, P. O. (2011). The Total Carbon Column Observing Network. *Philos. T. Roy. Soc. A*, *369*(1943), 2087–2112. doi:

10.1098/rsta.2010.0240
Yin, Y., Bloom, A. A., Worden, J., Saatchi, S., Yang, Y., Williams, M., . . . Schimel, D. (2020). Fire decline in dry tropical ecosystems enhances decadal land carbon sink. *Nature Communications*, *11*(1), 1900. Retrieved from `https://doi.org/10.1038/s41467-020-15852-2` doi: 10.1038/s41467-020-15852-2
Yin, Y., Chevallier, F., Ciais, P., Broquet, G., Fortems-Cheiney, A., Pison, I., & Saunois, M. (2015, dec). Decadal trends in global CO emissions as seen by MOPITT. *Atmospheric Chemistry and Physics*, *15*(23), 13433–13451. Retrieved from `http://www.atmos-chem-phys.net/15/13433/2015/acp-15-13433-2015.html` doi: 10.5194/acp-15-13433-2015
Yin, Y., Ciais, P., Chevallier, F., van der Werf, G. R., Fanin, T., Broquet, G., . . . Wang, Y. (2016). Variability of fire carbon emissions in Equatorial Asia and its non-linear sensitivity to El Niño. *Geophysical Research Letters*. Retrieved from `http://doi.wiley.com/10.1002/2016GL070971` doi: 10.1002/2016GL070971
Yoshida, Y., Joiner, J., Tucker, C., Berry, J., Lee, J.-E., Walker, G., . . . Wang, Y. (2015). The 2010 Russian drought impact on satellite measurements of solar-induced chlorophyll fluorescence: Insights from modeling and comparisons with parameters derived from satellite reflectances. *Remote Sensing of Environment*, *166*, 163–177.
Zhang, Y., Xiao, X., Zhou, S., Ciais, P., McCarthy, H., & Luo, Y. (2016). Canopy and physiological controls of GPP during drought and heat wave. *Geophysical Research Letters*, *43*(7), 3325–3333.
Zheng, B., Chevallier, F., Yin, Y., Ciais, P., Fortems-Cheiney, A., Deeter, M. N., . . . Zhao, Y. (2019, sep). Global atmospheric carbon monoxide budget 2000–2017 inferred from multi-species atmospheric inversions. *Earth System Science Data*, *11*(3), 1411–1436. Retrieved from `https://www.earth-syst-sci-data.net/11/1411/2019/` doi: 10.5194/essd-11-1411-2019